Supporting Online Material for

Coupled Pacific Rim megadroughts contributed to the fall of the Ming Dynasty's capital in 1644 CE

Materials and methods

Tree-ring data. During September, 2022, we collected increment cores from Chinese pine (*Pinus tabuliformis* Carr.) from six sampling sites in Beijing (Table S1). All the sampling was conducted in open stands growing on thin soils. Typically, two cores were extracted from each tree using increment borers. The increment cores were dried, mounted, polished and the tree-ring widths measured to the nearest 0.001 mm. The cross-dated ring width series were verified using the COFECHA program [1]. Considering the low canopy density and limited tree-tree competition, we first used the ARSTAN program [2] to detrend the cross-dated ring width sequences using a negative exponential curve. Core indices were computed as the ratio of the measured ring width to the fitted growth curve and were then averaged together (bi-weighted mean) to produce the regional chronology (RC). To reduce the potential influence of the variable sample length, we stabilized the variance of the chronology using the method described by Osborn et al [3]. To ensure a sufficient common signal within the chronology, the RC chronology used in the precipitation reconstruction described below was truncated prior to the period when the expressed population signal (EPS) [4] was > 0.85. The three tree climate record species extracted by principal component analysis (PCA) were *Pinus tabuliformis* Carr. [5,6,7].

Climate data. Beijing is one of the earliest cities in China to conduct modern meteorological observations. Monthly precipitation data were obtained from the Beijing station, which represent natural precipitation, covering the periods 1841–1855, 1859–1861, 1869–1884, 1886, 1890–1900, 1905–1908, 1910–1911, and 1914–2022 (Table S1). Average annual precipitation is 631 mm, and the total June–August precipitation (477.8 mm) accounts for 75.8% of the annual precipitation. The highest precipitation is in August, at 251 mm, and the lowest is in December, at 3 mm. Additionally, the gridded monthly climate dataset (1901–2022) of the Climatic Research Unit (CRU) TS 4.07 [8,9] was obtained from the web site: https://www.uea.ac.uk/groups-and-centres/climatic-research-unit/ (averaged over 39.5° N–41° N, 115.5° E–117.5° E). To determine the climate–tree growth relationships, correlations were calculated between the RC and seasonal total precipitation subsets from the previous September to the following August. There was a large amount of missing data from the Beijing meteorological station during the period 1841–1913, and therefore the correlations with the precipitation data were restricted to the period 1914–2022 (The mean value is 500 mm). Ultimately, we selected the CRU precipitation data for the precipitation reconstruction because it showed higher correlations with the tree-ring data than the station records, and because it provides a more regional signal.

Characteristics of the precipitation reconstruction

After correlating the RC chronology with the precipitation data (station and gridded), we found that the strongest correlation ($r = 0.67$, $P < 0.01$) was between the RC chronology and total August–June precipitation of the CRU, and significant correlation with total August–July precipitation of the CRU ($r = 0.65$, $P < 0.01$, 1914-

2022). Additionally, significant positive correlations with the PDSI and NDVI were found for April–July (r = 0.64, P < 0.01) and June-August (r = 0.56, P < 0.01). Using the RC chronology as the predictor, total August–July precipitation was chosen for the reconstruction. The reconstruction model accounts for 41.7% (r^2_{adj}=41.2%, P < 0.01) of the total variance in the instrumental precipitation over the calibration period from 1914 to 2022. The results of a split calibration–verification test revealed the good predictive skill of the regression model (Table S2). The reconstructed precipitation also shows significant correlations with total July–June precipitation of the CRU (r = 0.63, P < 0.01, 1914-2022) and total August–June instrumental precipitation (r = 0.57, P < 0.01, 1841–2022). Thus, the RC chronologyy also reflect the annual (water-year) total precipitation and greater hydroclimatic information. The reconstructed linear regression model is expressed as:

$$Y = 359.59 \times X + 148.27$$

where Y is the change in precipitation from August to July and X is the RC regional chronology. The reconstructed and 11-year running averaged total August–July precipitation for Beijing is shown in Figure 1C. The reconstruction shows substantial low-frequency precipitation variability during the period of 1550–2022. Several extended dry and wet periods (>11 years) were identified according to the 11-year running-averaged values of the precipitation reconstruction and the long-term mean (1550–2022, 508 mm). Dry periods occurred around 1576-1602, 1624-1647, 1734-1758, 1857-1870, 1897-1914, 1918-1950 and 1994-2010, and wet periods around 1648-1679, 1683-1716, 1759-1772, 1794-1813, 1817-1833, 1871-1896 and 1951-1965

(Table S3). As indicated by our precipitation reconstruction, the droughts during 1576–1593 and 1628–1644 were the most severe and long-lasting in Beijing since 1550 CE, and no annual precipitation attained the average level during these two megadroughts periods. Values beyond ±2 standard deviations (92 mm) indicate extremely dry and wet years, and on this basis, 9 extremely dry years and 13 extremely wet years are identified. Besides, the nine Garrisons of the Ming Dynasty were Liaodong, Xuanfu, Datong, Yansui, Ningxia, Gansu, Jizhou, Taiyuan and Guyuan.

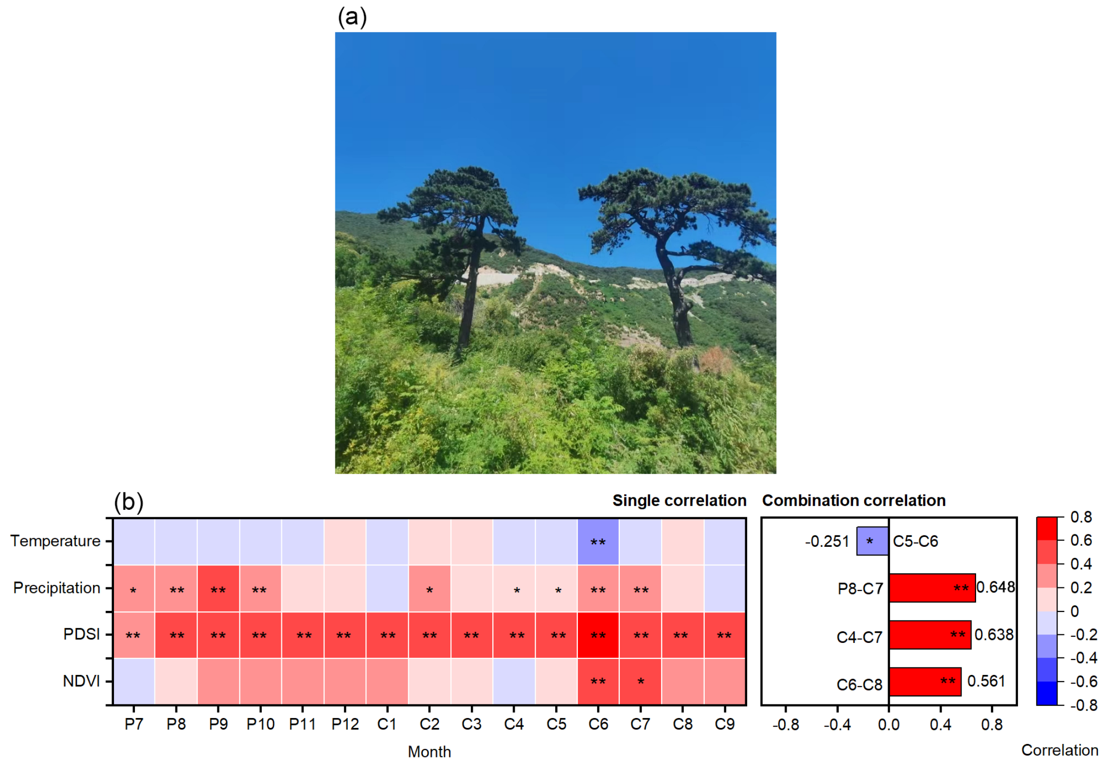

Fig. S1. (a) Sampling site (ZSY) in the Beijing. (b) Correlations between the regional chronology and mean monthly temperature, mean monthly precipitation, monthly PDSI and NDVI during the common periods (1914-2022 and 1982-2015). ** indicates significance at the 99% confidence level.

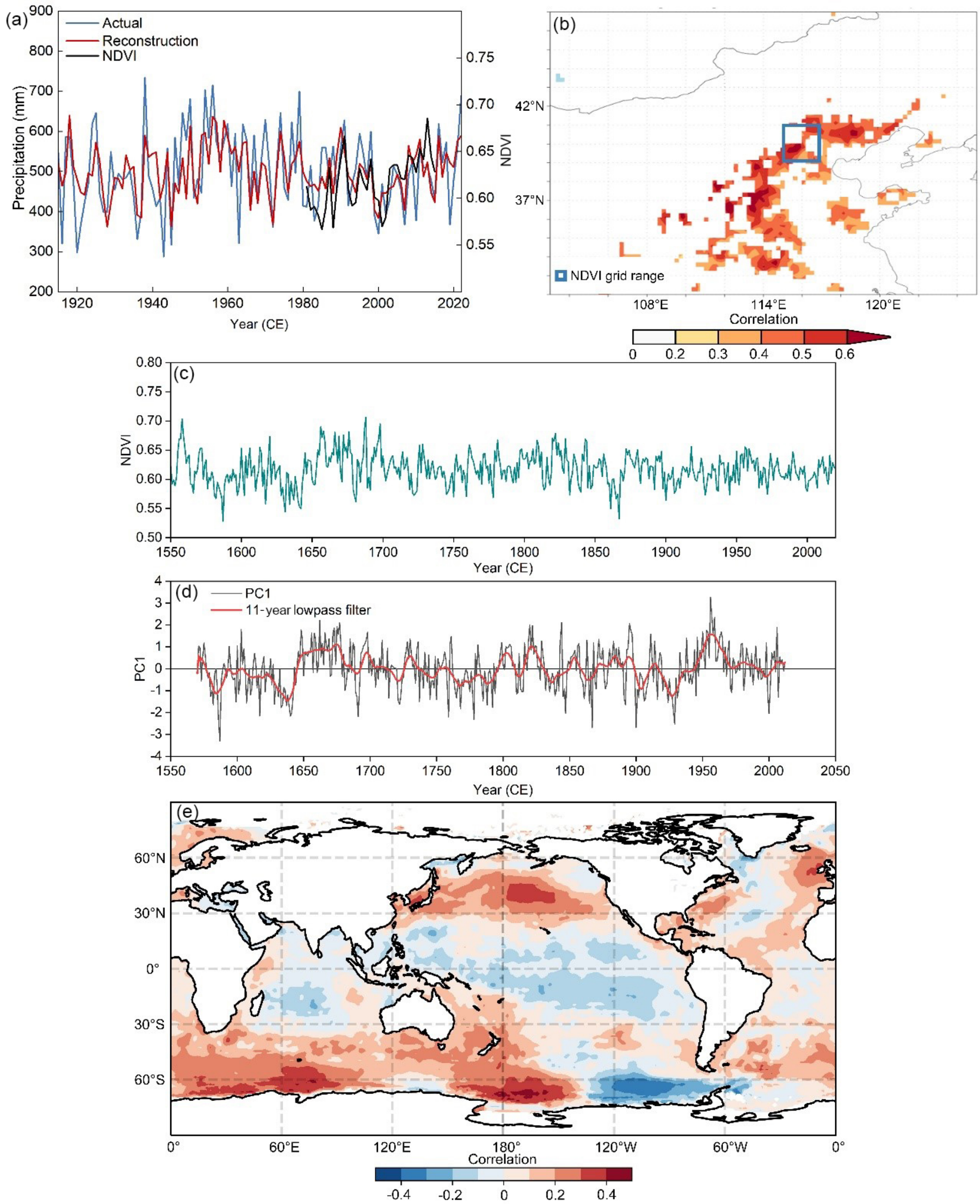

Fig. S2. (a) Comparison of actual and reconstructed total August–July precipitation for the period 1915–2022. (b) Spatial correlation patterns of PC1 with June-August NDVI for the period 1981–2015. (c) The tree ring estimates of June-August NDVI. (d) PC1 of several tree-ring records in northern China. (e) Spatial correlation patterns of PC1 with SSTs during the period 1870–2022.

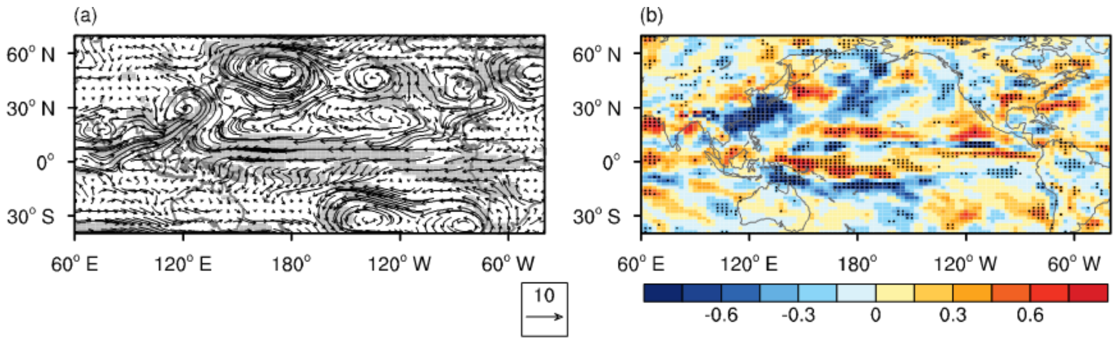

Fig. S3. CAM5 simulated differences in (a) vertically-integrated water vapor flux from 1000 to 100 hPa (vectors; units: kg m^{-1} s^{-1}) and (b) its divergence (shading; units: 10^{-5} kg m^{-2} s^{-1}) during the boreal summer (May–September) between the sensitivity simulation and control simulation. Areas with statistical significance exceeding the 90% confidence level are denoted by dots or grey shading.

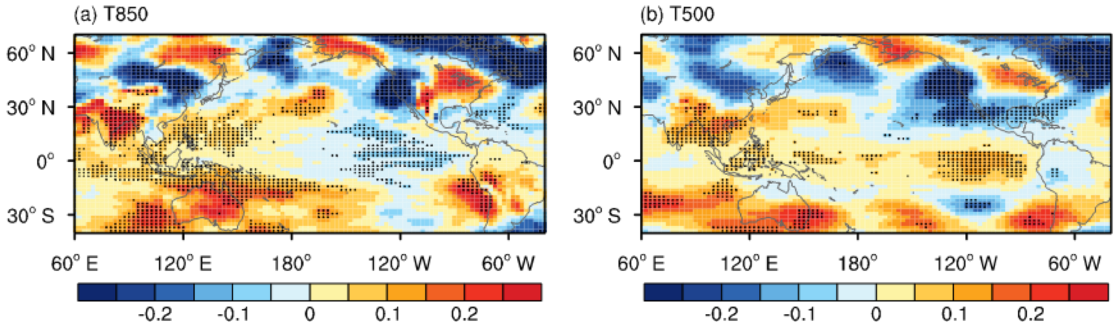

Fig. S4. CAM 5 simulated differences in air temperature at (A) 850 hPa and (B) 500 hPa (units: °C) during boreal summer (May–September) between the sensitivity simulation and the control simulation. Areas with statistical significance exceeding the 90% confidence level are denoted by dots.

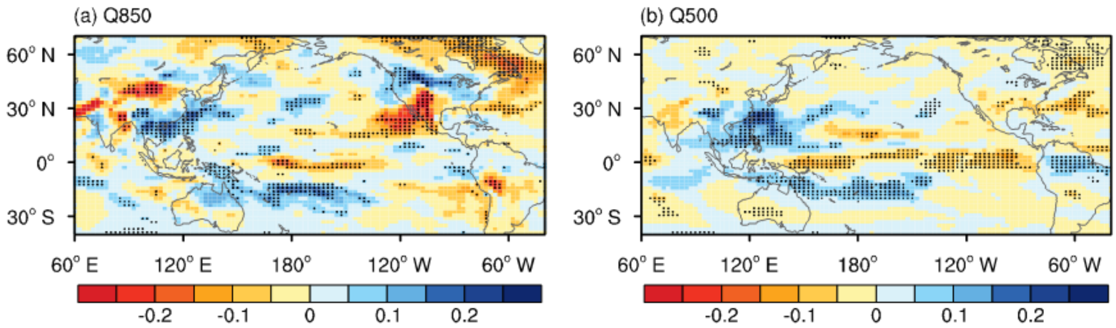

Fig. S5. CAM 5 simulated differences in specific humidity at (a) 850 hPa and (b) 500 hPa (units: 10^{-3} kg kg^{-1}) during boreal summer (May–September) between the sensitivity simulation and control simulation. Areas with statistical significance exceeding the 90% confidence level are denoted by dots.

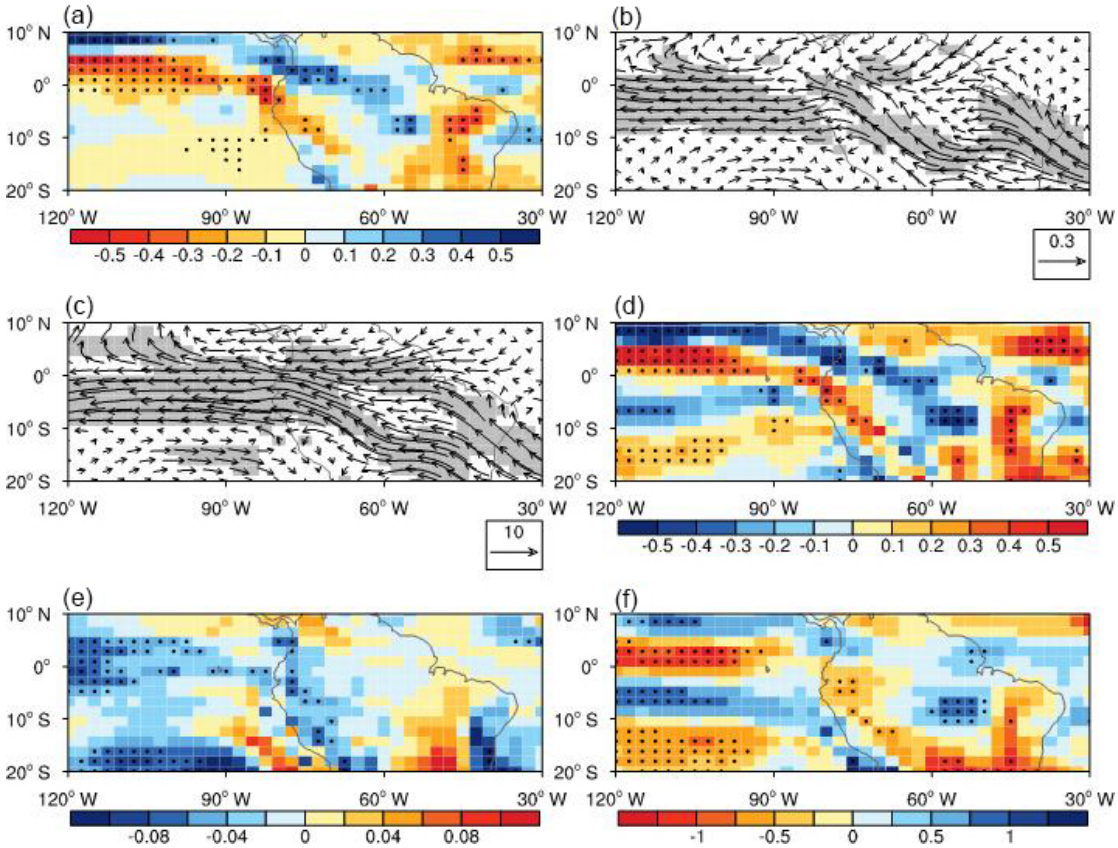

Fig. S6. CAM 5 simulated differences in (a) precipitation (units: mm d^{-1}), (b) wind field at 850 hPa (units: m s^{-1}), (c) vertically-integrated water vapor flux from 1000 to 100 hPa (units: kg m^{-1} s^{-1}) and (d) its divergence (units: 10^{-5} kg m^{-2} s^{-1}), (e) 850 hPa temperature (units: °C), (F) 850 hPa specific humidity (units: 10^{-4} kg kg^{-1}) during austral summer (November–March) between the sensitivity simulation and control simulation. Areas with statistical significance exceeding the 90% confidence level are denoted by dots or grey shading.

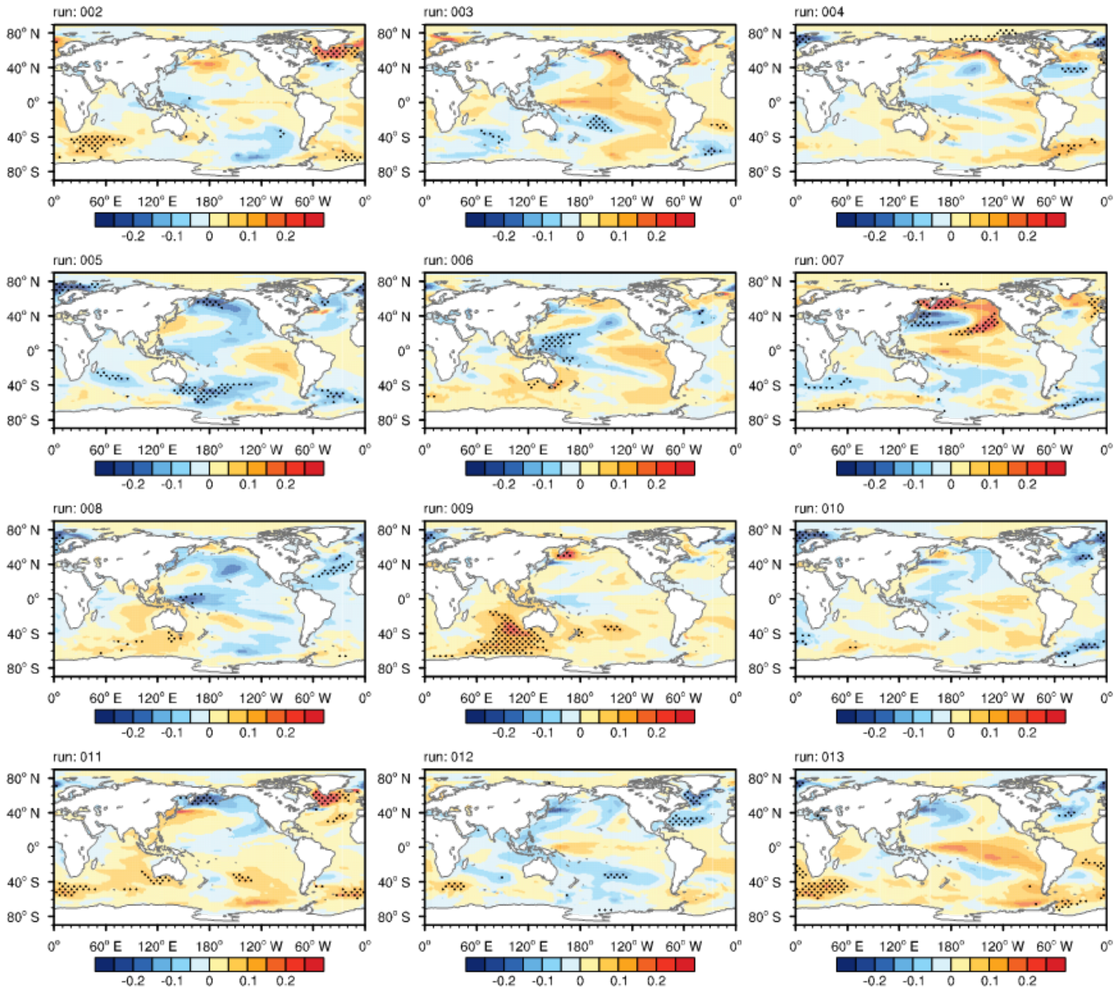

Fig. S7. Twelve CESM-LME all-forcing runs simulating annual SST anomalies (unit: ºC) during the period of 1576–1644 compared to the mean of the period 1550–1850. Areas with statistical significance exceeding the 90% confidence level are denoted by dots.

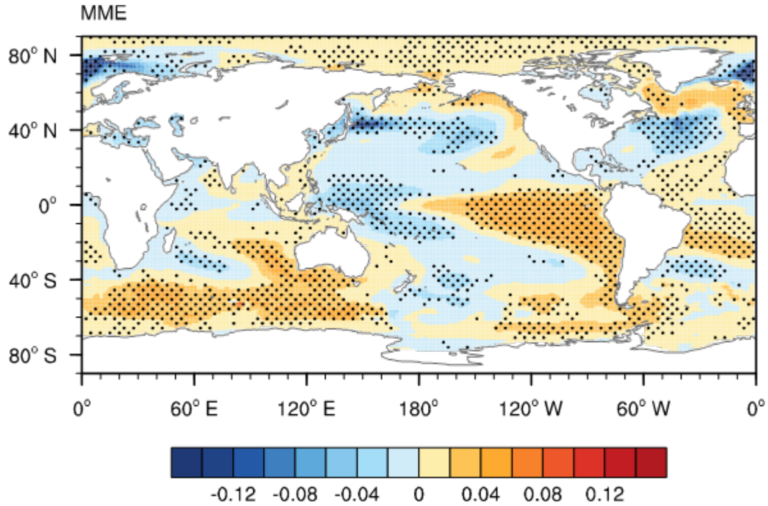

Fig. S8. Ensemble mean of the twelve CESM-LME all-forcing runs simulating annual SST anomalies (unit: ºC) during the period of 1576–1644 compared to the mean of the period 1550–1850. Areas where at least two-thirds (8 runs) of the total runs agreed on the sign of the ensemble mean are indicated by dots.

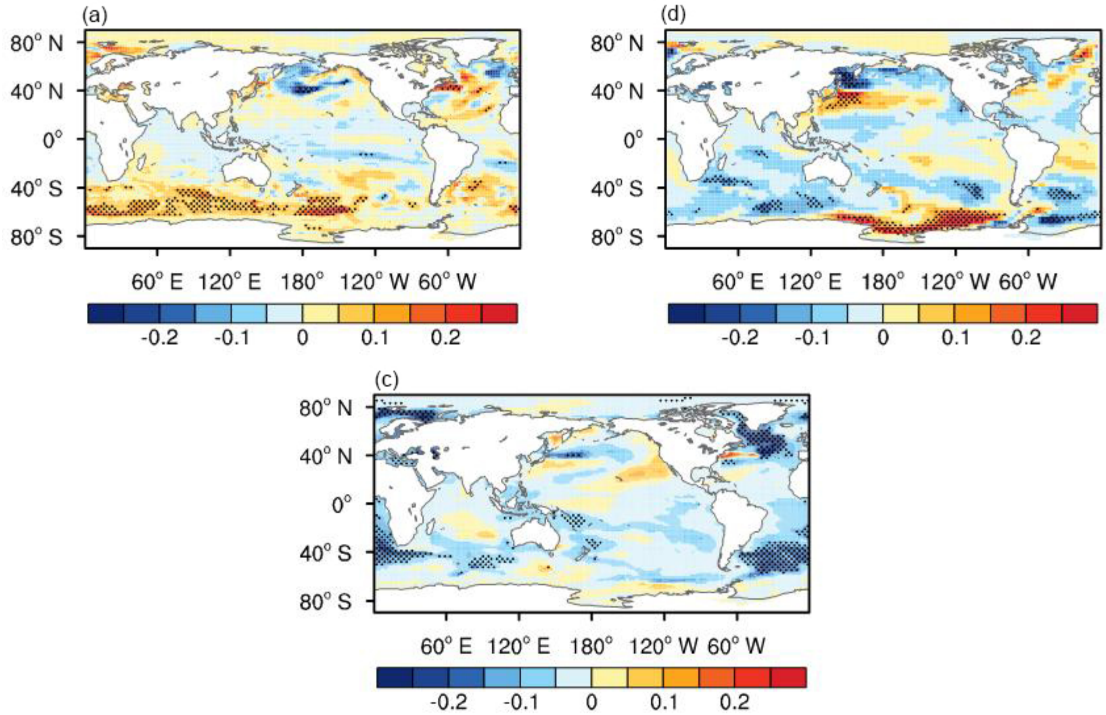

Fig. S9. Three PMIP4 coupled model simulations of annual SST anomalies (unit: ºC) during the period of 1576–1644 compared to the mean of the period 1550–1849. (a) INM-CM4-8, (b) MIROC-ES2L, (c) MRI-ESM2-0. Areas with statistical significance exceeding the 90% confidence level are denoted by dots.

Table S1. Site information for the standardized tree-ring chronologies. (The location of the corresponding climate station is shown in Fig. 1.)

Site	Lat. (N)	Long. (E)	Elevation (m)	Core/Tree number	Length	Mean sensitivity	Standard deviation	Correlation with the master series
QXM	40.56°	115.65°	1349	28/16	1525-2022			
ZSY	39.93°	116.01°	598	12/4	1600-2022			
YDS	40.55°	115.87°	925	50/25	1804-2022			
HBZ	39.92°	115.97°	732	50/25	1731-2022			
XLM	39.97°	115.47°	841	41/20	1625-2022			
XS	39.99°	116.06°	577	2/1	1523-1729			
RC				183/91	1523-2022	0.24	0.28	0.51
HJZ	36.37°	111.4°	1239		1520-2020			
Beijing	39.93°	116.28°	32		1841-2022			
CRU	39.5° - 41°	115.5° -117.5°			1914-2021			

Note: MS is the mean sensitivity; SD is the standard deviation; EPS is the expressed population signal.

Table S2. Calibration/verification statistics for the reconstructed total August–July precipitation

	Calibration (1915 – 1968)	Verification (1969 – 2022)	Calibration (1969 – 2022)	Verification (1915 – 1968)
r^2	0.420	0.416	0.416	0.420
ST_1		$37^+/17^-$**		38+/16^-**
ST_2		$37^+/16^-$**		$35^+/18^-$*
RE		0.417		0.440
CE		0.422		0.443

Note: r^2 is the coefficient of determination for the regression model fit to the combined years of the split-sample calibration and validation periods. ST_1 is the sign test; ST_2 is the first-order sign test; RE is the reduction of error; CE is the coefficient of efficiency. ** Significant at $P < 0.01$. * Significant at $P < 0.05$.

Table S3. Reconstructed precipitation wet and dry periods information

Dry periods	Precipitation (mm)	Wet periods	Precipitation (mm)
1576-1602	429.4	1648-1679	585.4
1624-1647	422.5	1683-1716	553.3
1734-1758	480.3	1759-1772	529.7
1857-1870	420.2	1794-1813	561.0
1897-1914	458.8	1817-1833	559.8
1918-1950	488.0	1871-1896	544.8
1994-2010	475.1	1951-1965	553.7

References

[1] Holmes RL. Computer-assisted quality control in tree-ring dating and measurement. Tree Ring Bull 1983; 43: 69-75.

[2] Cook ER. A Time-series Analysis Approach to Tree-ring Standardization. Ph.D. Thesis. USA, Tucson, University of Arizona; 1985.

[3] Osborn TJ, Briffa KR, Jones PD. Adjusting variance for sample-size in tree ring chronologies and other regional-mean time-series. Dendrochronologia 1997; 15: 89-99.

[4] Wigley TM, Briffa KR, Jones PD. On the average value of correlated time series, with applications in dendroclimatology and hydrometeorology. J Appl Meteorol Climatol 1984; 23: 201-213.

[5] Chen F, Opała-Owczarek M, Owczarek P, et al. Summer monsoon season streamflow variations in the middle Yellow River since 1570 CE inferred from tree rings of *Pinus tabulaeformis*. Atmosphere-Basel 2020; 11: 717.

[6] Zhang Y, Tian Q, Guillet S, et al. 500-yr. precipitation variability in Southern Taihang Mountains, China, and its linkages to ENSO and PDO. Clim Change 2017; 144: 419-432.

[7] Li Q, Deng Y, Wang S, et al. A half-millennium perspective on recent drying in the eastern Chinese Loess Plateau. Catena 2022; 212: 106087.

[8] Harris IPDJ, Jones PD, Osborn TJ, et al. (2014). Updated high‐resolution grids of monthly climatic observations-the CRU TS3. 10 Dataset. Int J Climatol 2014; 34: 623-642.

[9] van der Schrier G, Barichivich J, Briffa KR, et al. A scPDSI-based global data set of dry and wet spells for 1901-2009. J Geophys Res-Atmos 2013; 118: 4025-4048.